Article

Preparation of Spherical $\delta-MnO_2$ Nanoflowers by One-Step Coprecipitation Method as Electrode Material for Supercapacitor

Dazhi Zhang, Jiamian Dai, Jiajia Zhang, Yixin Zhang, Honglai Liu, Yunhui Xu, Jianjun Wu,* and Peipei Li*

Cite This: *ACS Omega* 2024, 9, 18032−18045

Read Online

| ACCESS | Metrics & More | Article Recommendations | Supporting Information |

ABSTRACT: Spherical δ-MnO$_2$ nanoflower materials were synthesized via a facile one-step coprecipitation method through adjusting the molar ratio of KMnO$_4$ to MnSO$_4$. The influence of the molar ratio of the reactants on the crystal structure, morphology, and electrochemical performances was investigated. At a molar ratio of 3.3 for KMnO$_4$ to MnSO$_4$, the spherical δ-MnO$_2$ nanoflowers composed of nanosheets with the highest specific surface area (228.0 m^2 g^{-1}) were obtained as electrode materials. In the conventional three-electrode system using 1 M Na$_2$SO$_4$ as an electrolyte, the specific capacitance of the spherical δ-MnO$_2$ nanoflowers reached 172.3 F g^{-1} at a current density of 1 A g^{-1}. Moreover, even after 5000 cycles at a current density of 5 A g^{-1}, the GCD curves remained essentially unchanged, and the specific capacitance still retained 86.50% of the maximum value. The kinetics of the electrode reaction were preliminarily studied through the linear potential sweep technique to observe diffusion-controlled contribution toward total capacitance. For the spherical δ-MnO$_2$ nanoflower electrode material, diffusion-controlled contribution accounted for 65.1% at low scan rates and still remained significant at high scan rates (100 mV s^{-1}), indicating excellent utilization efficiency of the bulk phase. The as-fabricated asymmetric supercapacitor HFC-7//MnO$_2$-3.3-ASC presented a prominent specific energy of 16.5 Wh kg^{-1} at the specific power of 450 W kg^{-1}. Even when the specific power reached 9.0 kW kg^{-1}, the energy density still retained 9.5 Wh kg^{-1}.
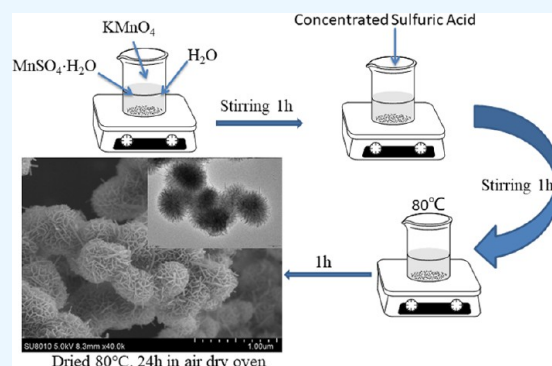
1. INTRODUCTION

Energy demand is on the rise due to the rapid global population and economic growth. Traditional fossil fuels, such as coal, oil, and natural gas, are increasingly being depleted as a result of human overexploitation and can no longer suffice the needs of a rapidly developing society. Fossil fuels emit significant amounts of carbon dioxide and other harmful gases during combustion, thereby accelerating the global greenhouse effect and causing severe damage to the ecological environment.[1−3] Consequently, scientific research is increasingly focused on transforming energy application techniques while exploring and developing new forms of energy conversion and high-performance energy storage devices. Supercapacitors, also known as electrochemical capacitors, hold great potential as energy storage devices owing to their high power density, rapid charge−discharge capabilities, long cycle life span, and considerable energy density.[4] Supercapacitors are widely used in hybrid electric vehicles, consumer electronics, aerospace, electromagnetic high-powered weapons, and various fields.[5]

Compared to carbon-based double-layered capacitors, pseudocapacitors utilize cost-effective manganese oxides to enhance the specific capacitance and energy density on the same electrode surface.[6] Recent studies have extensively investigated the potential of manganese dioxide (MnO$_2$)

nanomaterials as ideal supercapacitor electrode materials due to their significant theoretical specific capacitance (∼1370 F g^{-1}), superior thermal stability, abundant natural reserves, environmental friendliness, and low manufacturing cost.[7] MnO$_2$ primarily exists in six polymorphic forms, all consisting of the basic structural unit of the MnO$_6$ octahedron. Different arrangements of these octahedrons result in various polymorphic structures such as α-, β-, γ-, δ-, λ-, etc.[6,9−13] Numerous studies have demonstrated that the electrochemical performance of these MnO$_2$ polymorphs is significantly influenced by atomic arrangements leading to variations in surface characteristics, pore size distribution, and channel sizes.[14,15] To enhance charge storage capacity for MnO$_2$-based electrode materials, researchers have employed different synthesis techniques to fabricate various nanostructures including nanoparticles, nanorods, nanowires, nanourchins, and nanotubes with controllable morphologies, hierarchical porous structures, larger pore sizes,
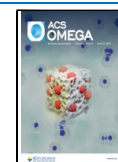
and substantial specific surface areas.[16−20] Zhang et al.[21] compared the electrochemical properties of various MnO_2 Nano morphologies prepared via direct precipitation, revealing that the specific capacitance changed in the following order: β- < γ- < δ- < α-MnO_2. Ghodbane et al.[22] synthesized different MnO_2 crystal phases using the wet chemical method, demonstrating relative specific capacitance of pyrolusite < Ni−todorokite < ramsdellite < cryptomelane < Ni-doped todorokite < birnessite < spinel.

The electrochemical performance of MnO_2 electrode materials, including specific capacitance, rate capacity, and cyclic stability, can be enhanced by considering various key factors, such as morphology, size, crystal structure, crystallinity, and conductivity. Although the use of hard or soft templates is typically necessary to achieve the desired morphology, crystallinity, and microstructure in MnO_2 electrode materials, it remains challenging to fully control the size, shape, and uniformity of MnO_2 nanostructures,[23−26] while template removal poses difficulties.

This study successfully synthesized three-dimensional (3D) δ-MnO_2 nanospheres through the in situ redox reaction between potassium permanganate and manganese sulfate monohydrate in an acidic aqueous solution, employing an environmentally friendly, cost-effective, and straightforward technique. The formation of δ-MnO_2 nanospheres occurred via the aggregation of nanosheets. The increased specific surface area and presence of pores among the nanosheets facilitated electrolyte−electrode material contact, thereby enhancing electrolyte ion diffusion and augmenting active site availability to enhance capacitive performance.

2. EXPERIMENTAL SECTION

2.1. Materials. Potassium permanganate (ACS reagent, $KMnO_4$), manganese sulfate monohydrate (ACS reagent, $MnSO_4 \cdot H_2O$), acetylene black (XFNANO, 30−45 nm), poly(vinylidene fluoride) (PVDF, average M_w ~ 534,000, powder, RG), and N-methyl pyrrolidone (NMP, AR, > 99.5%) were procured from Sigma−Aldrich Co. Ltd., while the concentrated sulfuric acid and sodium sulfate were provided by Nanjing Chemical Reagent Co. Ltd. All chemicals were of analytical purity and utilized without any additional purification.

2.2. Synthesis of δ-MnO_2 Nanoflowers. The spherical δ-MnO_2 nanosheet structures were obtained through a simple chemical coprecipitation method. In a three-necked flask, $KMnO_4$ (2.016 g), $MnSO_4 \cdot H_2O$ (0.654 g), and deionized water (100 mL) were added and continuously mechanically stirred for 1 h. Then, 2.5 mL of concentrated sulfuric acid was gradually added, and the mixture was stirred for another hour. The mixture was heated to 80 °C in a water bath and vigorously stirred for an additional 1 h until the reaction was completed. The resulting solution was filtered and washed with deionized water until the pH of the filtrate reached 7, followed by drying the filter cake in an oven at 80 °C for 24 h. The designated product was named MnO_2-3.3, where 3.3 represented the molar ratio of $KMnO_4$ to $MnSO_4 \cdot H_2O$ used in the synthesis process. The samples MnO_2-2.5 and MnO_2-5.7 were prepared using the same synthesis process but with different molar ratios of $KMnO_4$ to $MnSO_4 \cdot H_2O$. Figure 1 illustrates a schematic representation of δ-MnO_2 preparation via the chemical method. Table 1S presents information about dosages as well as molar ratios of $KMnO_4$ and $MnSO_4 \cdot H_2O$.

2.3. Characterization. The X-ray diffraction (XRD) patterns were obtained using a Bruker D8 Advance diffrac-
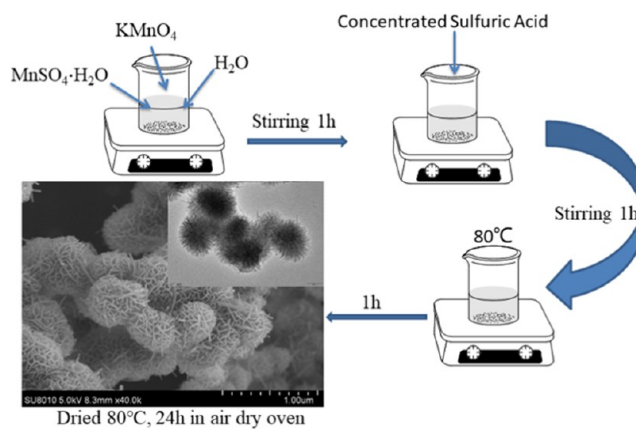

Figure 1. Schematic diagram for the preparation of spherical δ-MnO_2 nanoflowers.

tometer equipped with monochromatized Cu Kα radiation (λ = 1.5406 Å) operated at 40 kV with a scan rate of $10°$ min^{-1} and step size of $0.02°$. Scanning electron microscopy (SEM, Zeiss GeminiSEM 500, Germany) and transmission electron microscopy (TEM, FEI, Tecnai G2 F20) were applied to examine the structures and morphologies of the samples. The surface elemental composition and chemical valence state were acquired by X-ray photoelectron spectroscopy (XPS, Thermo Fisher Scientific ESCALAB 250Xi) with a monochromatic Al Kα X-ray source. The isotherms of nitrogen adsorption−desorption were obtained using the Autosorb iQ2 (Quantachrome) physisorption analyzer. The specific surface area was determined utilizing the multipoint BET theoretical model, while micropore area and volume were determined employing the T-plot method. Total pore volume calculation relied on the amount of nitrogen adsorbed at a relative pressure P/P_0 = 0.99, and pore diameter distribution analysis was conducted using density function theory (DFT).

2.4. Electrochemical Measurements. The MnO_2-R, synthesized at various molar ratios of $KMnO_4$ to $MnSO_4$, was employed as a supercapacitor electrode in a three-electrode system for investigating its electrochemical performance in a 1 M Na_2SO_4 electrolyte. The working electrode was prepared by grinding acetylene black, the electrode material, and PVDF dispersion liquid (1:8:1 wt %) together before coating the pre-prepared nickel foam (1 cm × 1 cm) with the mixture and drying it at 80 °C for 24 h. The active material coating on nickel foam was approximately 2.4 mg. Platinum sheet (1 cm × 1 cm) and saturated calomel (SCE) electrodes were utilized as counter and reference electrodes, respectively. The electrochemical workstation (CHI 660E, Shanghai, China) was utilized to conduct the electrochemical performances, such as cyclic voltammetry (CV), galvanostatic charge−discharge (GCD), and electrochemical impedance spectroscopy (EIS). The specific capacitance was determined by analyzing the discharging curve with eq 1

$$C = \frac{I\Delta t}{m\Delta u} \tag{1}$$

I (A) is the applied current, Δt (s) is the discharge time, m (g) is the active material mass, and Δu (V) is the discharging potential window.

3. RESULTS AND DISCUSSION

Figure 2 illustrates the XRD patterns of both experimental MnO_2 and a commercially obtained reference sample from
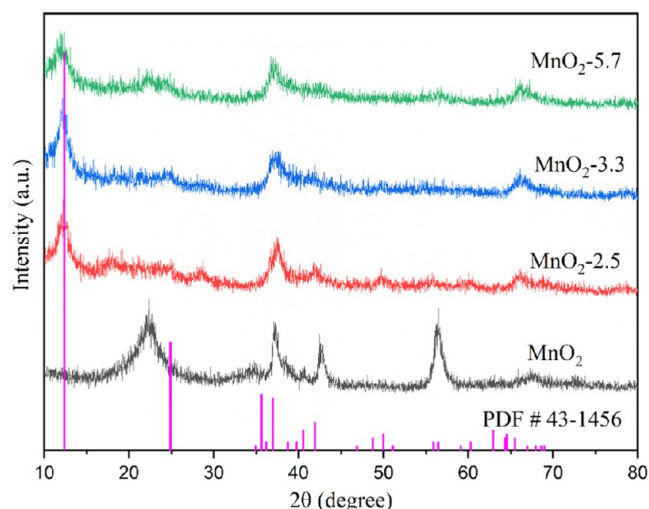

Figure 2. XRD patterns for three prepared MnO_2 and reference substance MnO_2.

Sinopharm Chemical Reagent Co. Ltd. The synthesized MnO_2 at various molar ratios exhibited comparable diffraction profiles,

while the diffraction peaks observed at $2\theta = 12.3, 24.9, 37.1,$ and $66.1°$ corresponded to crystal planes (001), (002), (006), and (119), respectively, which are associated with two-dimensional layered birnessite.[22] The δ-MnO_2 formation (JCPDS: 43−1456) was confirmed. It displayed a monoclinic system, a $C2/m$ space group, with cell parameters of $a = 5.174$ Å, $b = 2.850$ Å, $c = 7.336$ Å, and $\beta = 103.18°$.[21] The weak intensity of the diffraction peak indicated a low degree of crystallization for δ-MnO_2, while the broad diffraction peaks suggested small particle sizes. The XRD images of the MnO_2 reference substance exhibited four distinct diffraction peaks at 2θ values of 22.3, 37.1, 42.6, and 56.4°, corresponding to the (120), (131), (300), and (160) crystal planes of ramsdellite (JCPDS: 39−375),[21,22] respectively. The elemental composition and chemical valence states of prepared MnO_2 were characterized via XPS analysis (Figure 3). As depicted in Figure 3(a), the MnO_2-R electrode materials comprised manganese (Mn), oxygen (O), and carbon (C), with element C originating from carbon dioxide of the test atmosphere. Figure 3(b) illustrates the orbital spectrum of Mn 2p, where the peaks at 654.4 and 642.5 eV corresponded to Mn 2p1/2 and Mn 2p3/2, respectively, while a spin separation energy of 11.9 eV indicated that manganese existed in its +4 oxidation state within the material, confirming it as manganese dioxide (MnO_2).[27] The high-resolution XPS spectra of Mn $2p_{3/2}$ can be fitted to 641.4, 642.5, and 643.6 eV, as shown in Figure 3 (c), which belong to Mn^{2+}, Mn^{3+}, and Mn^{4+},[28] respectively. Figure 3 (d) shows the fine spectrum of O 1s. It can be seen that
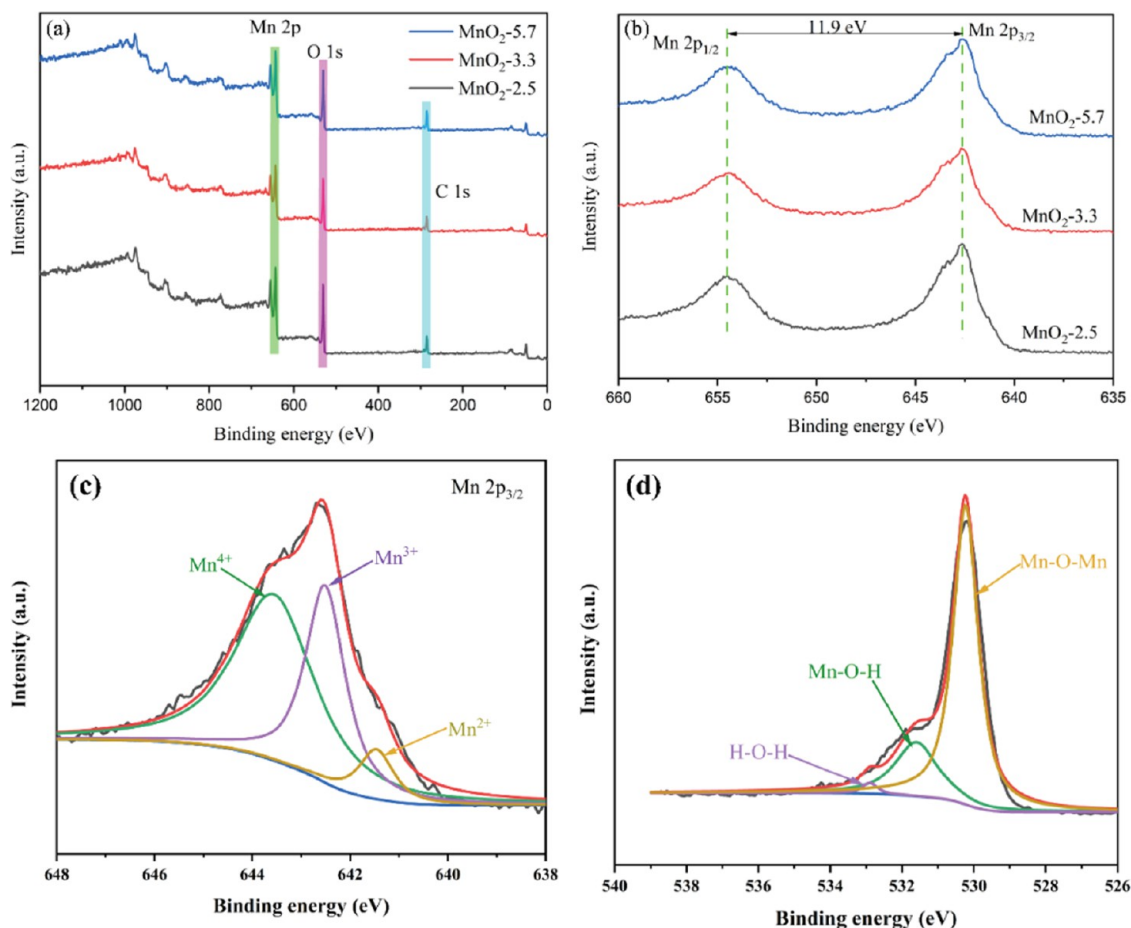

Figure 3. XPS spectra of the MnO_2-R electrode: (a) survey photoelectron spectra, (b) Mn 2p spectra, (c) high-resolution spectrum of Mn $2p_{3/2}$, and (d) high-resolution spectrum of O 1s.
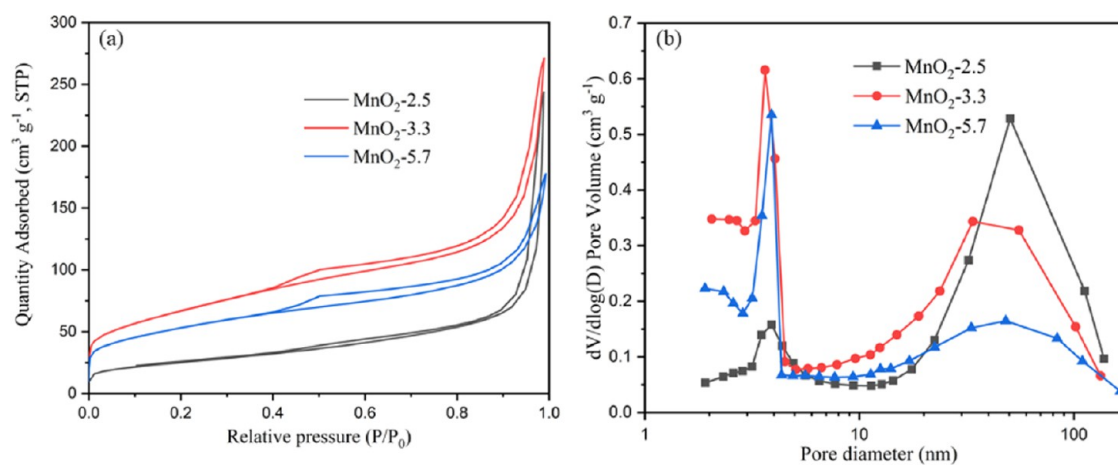
Figure 4. (a) Nitrogen adsorption/desorption isotherms and (b) the pore size distribution curves of the MnO_2-R electrodes.
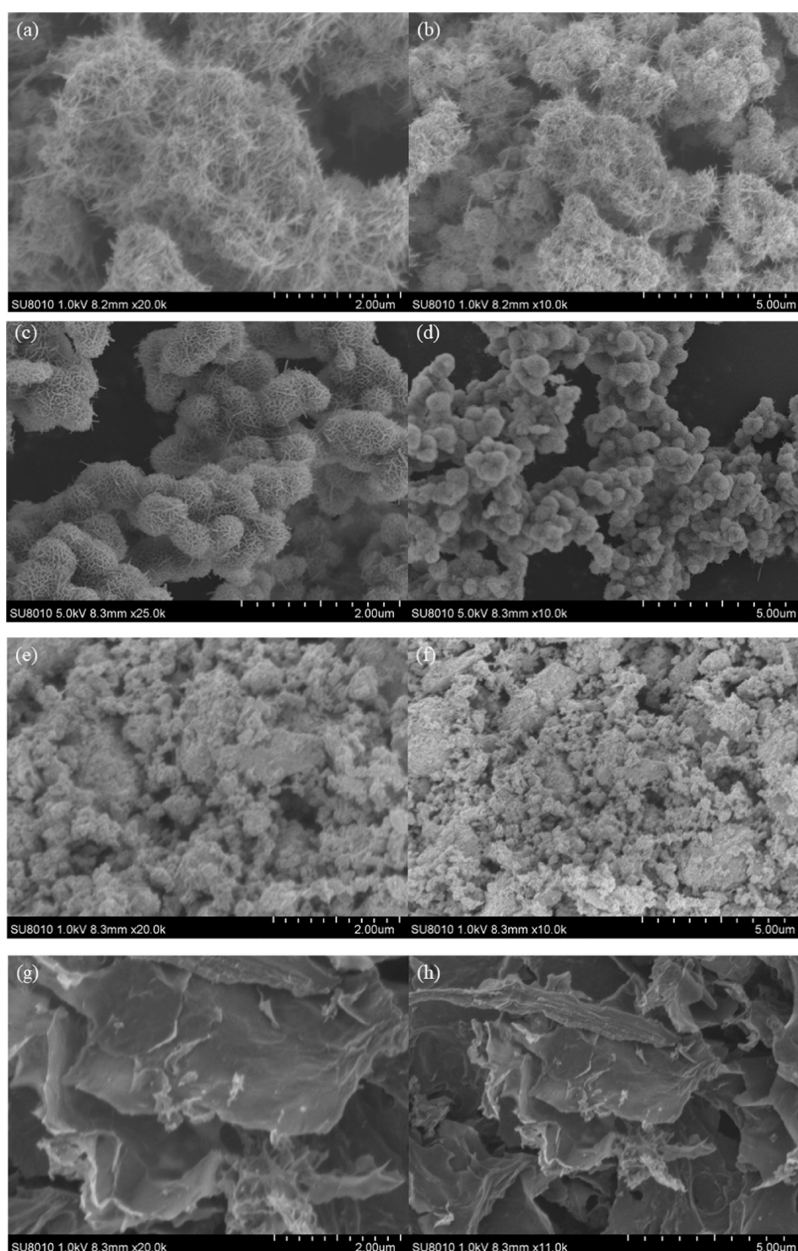

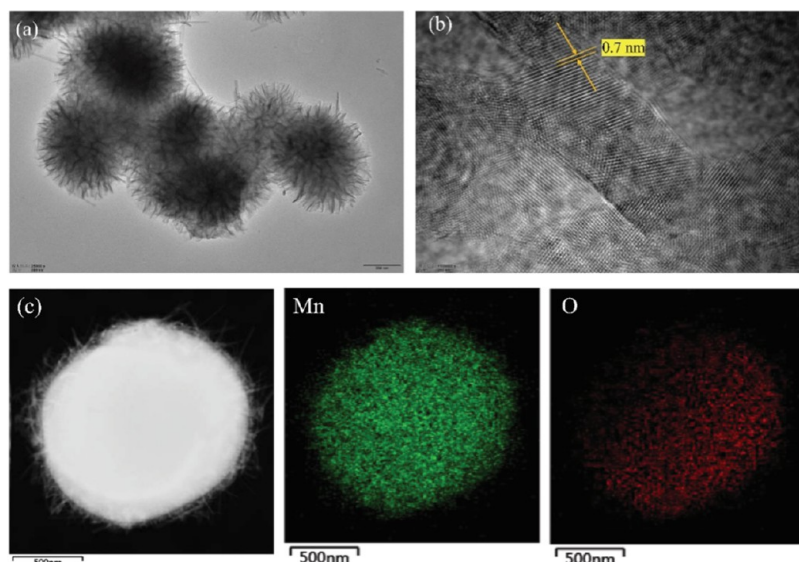**Figure 5.** SEM images of (a, b) MnO_2-2.5, (c, d) MnO_2-3.3, (e, f) MnO_2-5.7, and (g, h) reference substance MnO_2.

Figure 6. (a) TEM image of MnO$_2$-3.3, (b) HRTEM image of MnO$_2$-3.3, and (c) element mapping images of MnO$_2$-3.3.
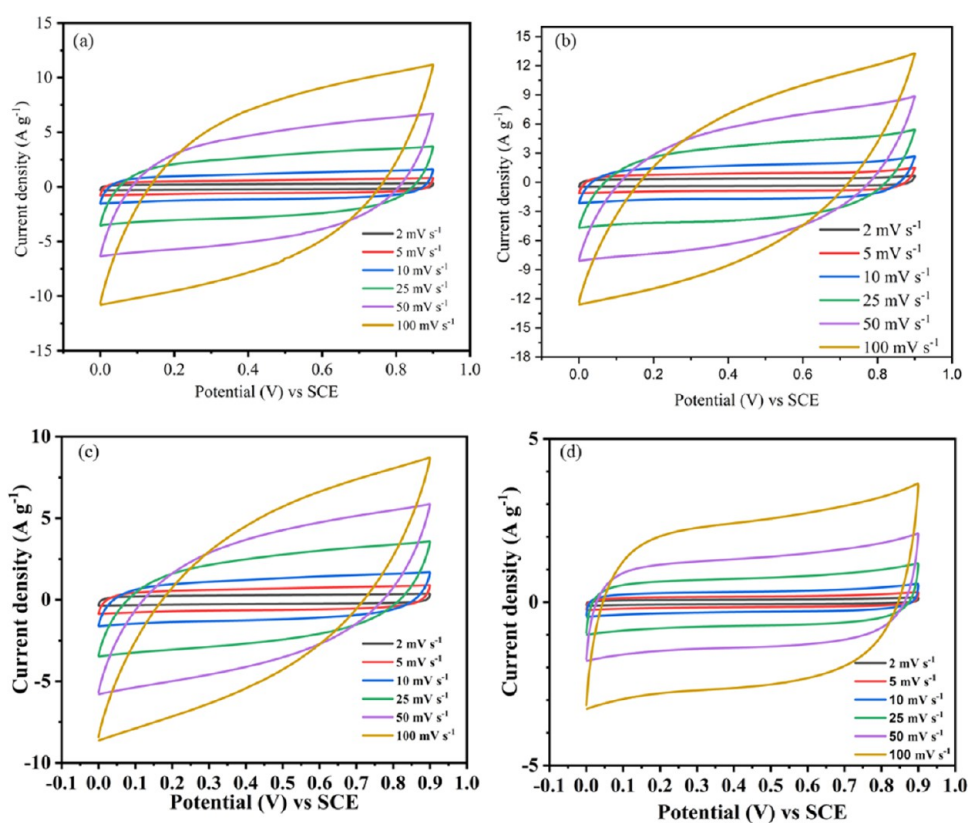
Figure 7. Cyclic voltammograms of (a) MnO$_2$-2.5, (b) MnO$_2$-3.3, (c) MnO$_2$-5.7, and (d) MnO$_2$ electrodes at different scan rates in a 1 M Na$_2$SO$_4$ aqueous system.

O 1s can be fitted to Mn−O−Mn (530.2 eV), Mn−OH (531.6 eV), and H−O−H (532.9 eV).[29,30]

The electrochemical properties of the MnO$_2$ materials are closely linked to their specific surface areas and pore size distribution patterns. In this experiment, the specific surface areas and pore structure parameters of the samples were analyzed through an N$_2$ adsorption−desorption test to investigate their impact on the product's electrochemical properties. Figure 4(a) displays the nitrogen adsorption−desorption isotherms of the MnO$_2$-R electrode materials,

which exhibited type IV isotherm characteristics with type H3 hysteresis loops (primarily corresponding to layered aggregates) at different molar ratios of KMnO$_4$ to MnSO$_4$, indicating a scarcity of micropores in the material and mostly medium-to-large pores.[31] The adsorption curve exhibited a sharp rise in the low-pressure region ($0.0 \leq P/P_0 \leq 0.1$), indicating the presence of a microporous structure in the MnO$_2$-R electrode material. In the medium-pressure region ($0.1 \leq P/P_0 \leq 0.8$), there was a gradual increase in the adsorption curve, suggesting a mesoporous structure, while in the high-pressure section (0.8

$\leq P/P_0 \leq 1.0$), there was a rapid ascent, indicating the existence of large pores in the MnO$_2$-R electrode material. The lower limit of the adsorption and desorption branches of the H3 hysteretic loop was observed at P/P_0 0.4, indicating a layered pore structure corresponding to δ-MnO$_2$ birnessite.[24] In addition, the δ-MnO$_2$ nitrogen adsorption capacity was significantly influenced by the molar ratio of KMnO$_4$ to MnSO$_4$. Experimental results showed that δ-MnO$_2$ nitrogen adsorption capacity was increased and then decreased with the increase of the ratio of KMnO$_4$ to MnSO$_4$. As presented in Table 2S, elevating the molar ratio of KMnO$_4$ to MnSO$_4$ from 2.5 to 3.3 led to an enhancement in the specific surface area of the subsequent MnO$_2$-R electrode material from 86.8 m^2 g^{-1} (MnO$_2$-2.5) to 228.0 m^2 g^{-1} (MnO$_2$-3.3). Nevertheless, further increasing the KMnO$_4$ level caused a reduction in the specific surface area of the MnO$_2$-R electrode materials from 228.0 to 179.6 m^2 g^{-1} (MnO$_2$-5.7). The pore size distribution curve of the MnO$_2$-R electrode materials (Figure 4(b)) revealed that the predominant pore structures in all three samples were mesopores, primarily around 4 and 50 nm, while micropores below 2 nm were found to be minimal.

The surface morphologies of MnO$_2$-R electrode materials were observed by using SEM technology. Figure 5(a,b) depicts the SEM images of δ-MnO$_2$ obtained at a KMnO$_4$ to MnSO$_4$ molar ratio of 2.5, revealing nest-like structures that exhibited a tendency to agglomerate into spherical formations. These nest-like structures consisted of nanowires with varying lengths and thicknesses. With an increase in the KMnO$_4$ to MnSO$_4$ molar ratio to 3.3 (Figure 5(c,d)), δ-MnO$_2$ formed relatively uniform sphere-like nanoflowers with an approximate diameter of 0.5 μm, composed primarily of nanosheets. Further elevation in the KMnO$_4$ level facilitated the formation of multiple forms of δ-MnO$_2$, which rapidly aggregated into chunks (Figure 5(e,f)). Figure 5(g,h) displays the SEM images of the reference substance MnO$_2$, exhibiting a rough and irregular flaky structure. The MnO$_2$-3.3 electrode was analyzed by using TEM technology to further investigate the microstructural characteristics, as shown in Figure 6(a). It exhibited a spherical nanoflower morphology, while δ-MnO$_2$ appeared as ultrathin individual nanosheets. This unique spherical nanostructure provided abundant electrochemically active surface sites for Faraday reactions and facilitated rapid ion transport, thereby promoting high specific capacitance and excellent capability rate. The HRTEM image (Figure 6(b)) revealed that the spherical MnO$_2$ nanosheets displayed a lattice structure with an average interlayer distance of 0.7 nm, corresponding to the crystal plane of δ-MnO$_2$ (001).[6] The element mapping image (Figure 6(c)) showed that Mn and O elements were evenly distributed on the nanosheet.

4. ELECTROCHEMICAL STUDIES

The CV curves of the MnO$_2$-R prepared at different molar ratios of KMnO$_4$ to MnSO$_4$ and the reference substance MnO$_2$ at various scanning rates are presented in Figure 7. All of the CV curves exhibited similar rectangular shapes without distinct redox peaks, indicating that the working electrodes maintained a quasi-constant charging and discharging rate across the entire voltage range. This suggested that all of the samples exhibited ideal capacitive behavior.[32] The current of each electrode correspondingly increased as the scanning rate was elevated from 2 to 100 mV s^{-1}, in accordance with the characteristic behavior exhibited by supercapacitors. Moreover, CV curves at different scanning rates consistently maintained an approx-

imately rectangular shape, indicating excellent capability rate performance and reversible charge storage processes of the samples. The integrated area of the CV curve can be utilized to determine the specific capacitance of the electrode material. At a scanning rate of 50 mV s^{-1}, spherical δ-MnO$_2$ nanoflower electrodes (MnO$_2$-3.3) demonstrated the largest area in their CV curves (as depicted in Figure 8), signifying superior
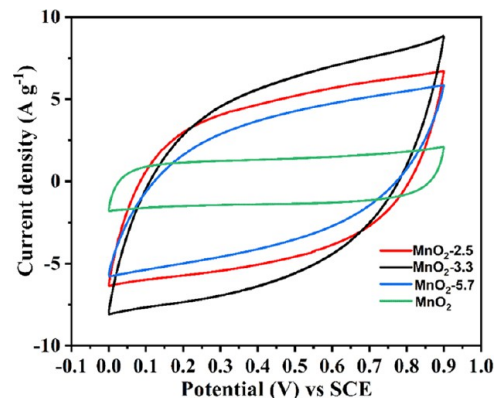

Figure 8. Cyclic voltammograms of MnO$_2$-R and MnO$_2$ electrodes at the scan rate of 50 mV s^{-1}.

capacitance performance. Furthermore, GCD technology was used to measure the capacitive properties of each sample at a current density of 1 A g^{-1}, and the results are shown in Figures 9 and 10. As can be seen from the figures, all of the GCD curves exhibited linear and typically symmetrical triangular behavior, indicating that the electrode displayed excellent capacitance. According to eq 1, the specific capacitance of each electrode at 1 A g^{-1} exhibited the following order: MnO$_2$ (26.7 F g^{-1}) < MnO$_2$-5.7 (97.4 F g^{-1}) < MnO$_2$-2.5 (104.5 F g^{-1}) < MnO$_2$-3.3 (172.3 F g^{-1}), which was consistent with the results obtained from CV testing. Table 1 presents the specific capacitance of different samples at various current densities. The Coulomb efficiency of all of the samples was close to 100%.

The δ-MnO$_2$ exhibited a two-dimensional layered configuration comprising alternating stacked Mn−O layers (edge-shared MnO$_6$ octahedra) and hydrated alkali metal cations (Na$^+$ and K$^+$).[33,34] Its fundamental structural unit consisted of a tightly and uniformly encircled Mn atom with six oxygen atoms (Figure 11(a)). Within each MnO$_6$ octahedral layer (Figure 11(b)), every Mn atom was also closely surrounded by six oxygen atoms along the c−axis, indicating an even distribution of Mn atoms in the layer. However, when viewed in Figure 11(c), the six oxygen atoms around the Mn atom were not coplanar, with three above and three below the Mn atom. Additionally, some cations, such as H$^+$, Na$^+$, K$^+$, and Ca^{2+}, were present between the layers. Figure 11(d) illustrates the birnessite crystal structure, revealing a layer spacing of 7 Å.[35] Due to the presence of cations in the interlayer region, manganese's oxidation state is not entirely quadrivalent; instead, it averages between 3.6 and 3.8, indicating predominantly Mn(IV) with a minor amount of Mn(III) in the birnessite structure.[36]

The formation of MnO$_2$ was facilitated by the coprecipitation of KMnO$_4$ and MnSO$_4$, as indicated by the following reaction formula

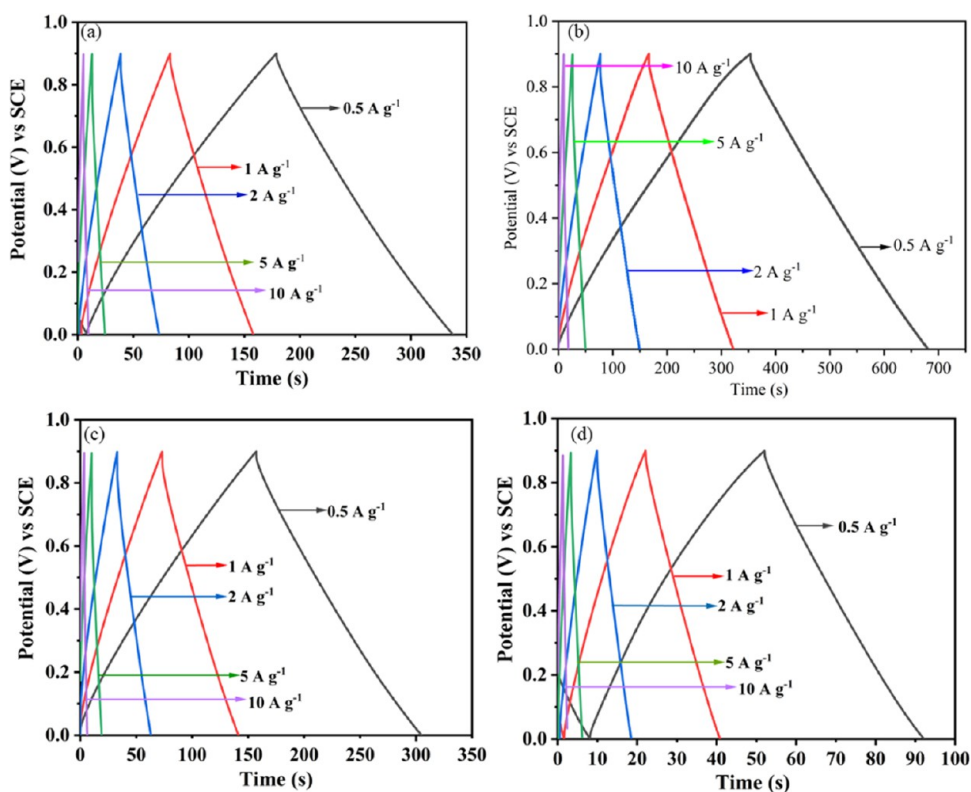$$2Mn^{7+} + 3Mn^{2+} \rightarrow 5Mn^{4+} \quad (2)$$
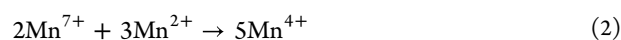
Figure 9. Galvanostatic charge–discharge curves at different current densities in the 1 M Na_2SO_4 aqueous system of (a) MnO_2-2.5, (b) MnO_2-3.3, (c) MnO_2-5.7, and (d) MnO_2.
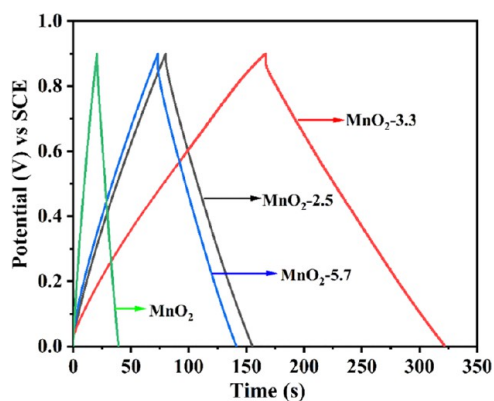

Figure 10. Galvanostatic charge–discharge curves of MnO_2-R and MnO_2 electrodes at a current density of 1 A g^{-1}.

Table 1. Specific Capacitance of MnO_2-R and MnO_2 Electrodes at Different Current Densities

	specific capacitance (F g^{-1})				
samples	0.5 (A g^{-1})	1 (A g^{-1})	2 (A g^{-1})	5 (A g^{-1})	10 (A g^{-1})
MnO_2-2.5	112.8	104.5	93.2	69	39.3
MnO_2-3.3	181.7	172.3	162	132.5	95.8
MnO_2-5.7	105.4	97.4	86.3	63.9	38.9
MnO_2	28.7	26.7	24.7	21	16.6

When the MnO_2 reached its critical nucleation size, it facilitated the formation of numerous crystal nuclei, subsequently aggregating into small grains due to Ostwald maturation and gradually growing into linear anisotropic structures. The growth rate of these linear anisotropic nanowires increased as the reaction progressed. Eventually, the anisotropic nanowires underwent gradual agglomeration, resulting in a spherical shape due to lower surface energy.[37] With a higher concentration of $KMnO_4$ (MnO_2-3.3), there was a rapid increase in MnO_2 production and a transition from nucleation dominance to growth dominance, leading to directional growth observed in the form of a spherical nanosheet. As the concentration of $KMnO_4$ continued to increase (MnO_2-5.7), the generated MnO_2 rapidly aggregated and exhibited large solid surface morphology with varying sizes.[38]

A series of EIS tests were conducted at various frequencies to evaluate the frequency response characteristics of MnO_2-R and the reference substance MnO_2. The results are presented in Figure 12(a). In comparison to other samples, the Nyquist plot of MnO_2-3.3 exhibited a nearly vertical line in the low-frequency region, indicating superior capacitance characteristics and a faster ion diffusion rate. As shown in the enlarged image inserted in Figure 12(a), all electrode materials displayed a semicircular arc in the high-frequency region, where these arcs intersected with the real axis represented their equivalent series resistance (R_s), which were measured as 2.08 Ω (MnO_2-5.7), 2.76 Ω (MnO_2), 2.97 Ω (MnO_2-3.3), and 3.18 Ω (MnO_2-2.5), respectively. The equivalent circuit model is fitted in Figure S1. Among them, MnO_2-3.3 exhibited a smaller semiarc diameter, indicating lower charge transfer resistance, which facilitated electrolyte ion diffusion. To investigate the cyclic stability of the spherical δ-MnO_2 nanoflower electrode, the MnO_2-3.3 electrode was tested at a current density of 5 A g^{-1} for 5000 repetitive GCD cycles. The changes of the specific capacitance are presented in Figure 12(b), demonstrating a gradual increase during the initial stage of the cycle, reaching 134.08 F g^{-1} at 1250 cycles, which can be attributed to the
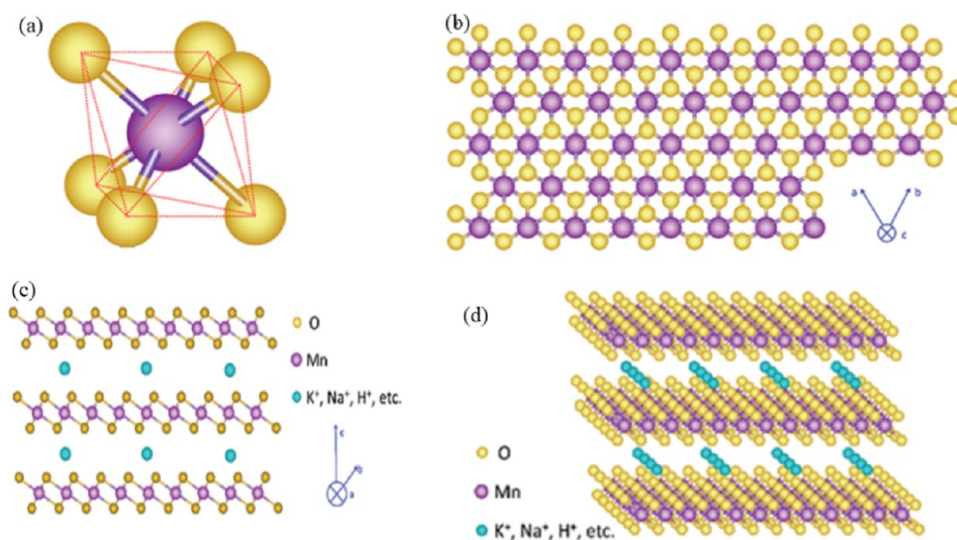
Figure 11. (a) MnO_6 octahedron unit; (b) schematic diagram of birnessite along the 001 plane; (c) schematic diagram of birnessite viewed along the 011 plane; (d) stereoscopic schematic diagram of birnessite.
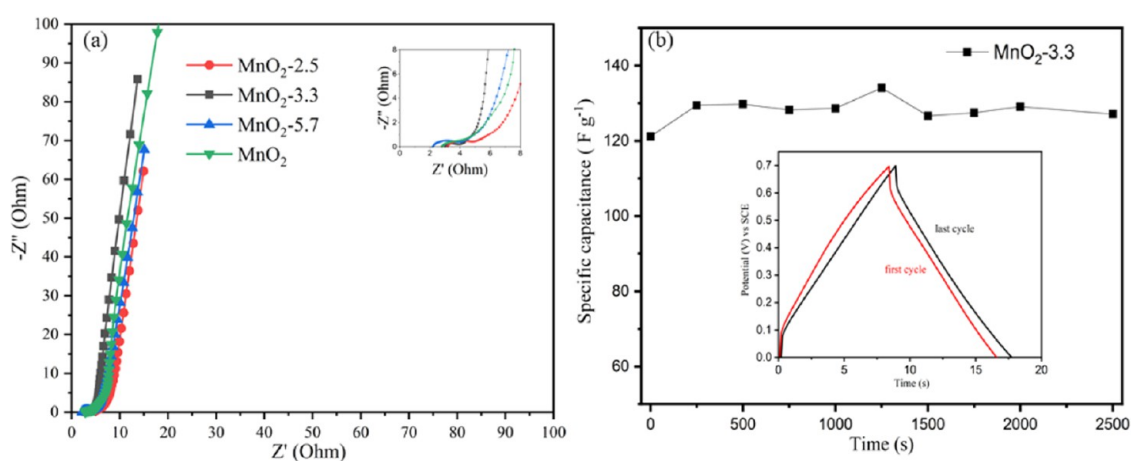

Figure 12. (a) Nyquist diagram of MnO_2-R and MnO_2 electrodes and (b) cycle life of MnO_2-3.3 electrode at 5 A g^{-1}.
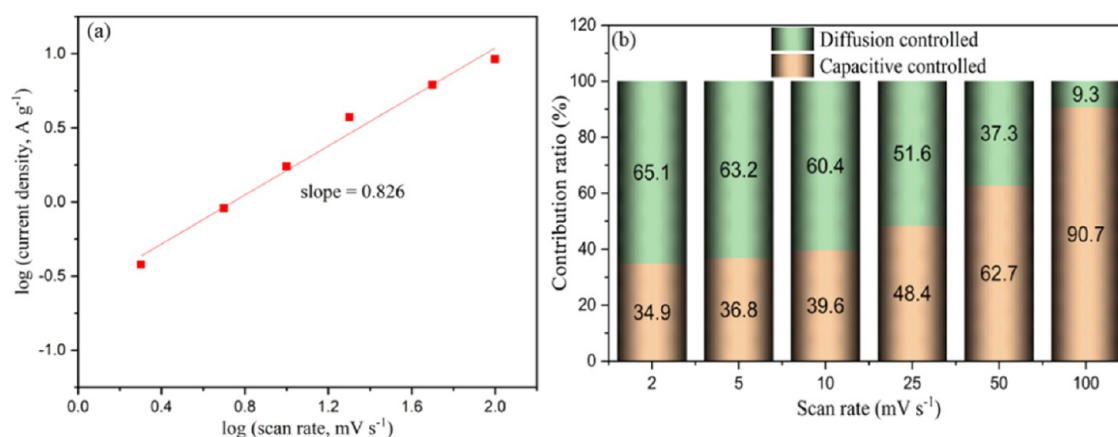

Figure 13. (a) Plots of log (current density) vs log (scan rate) for MnO_2-3.3 electrode and (b) normalized ratios of capacitive contribution and diffusion contribution for MnO_2-3.3 electrode.

activation of the electrode material. Subsequently, there was gradual attenuation; however, even after 5000 cycles, the specific capacitance still retained 86.5% of its maximum value. No significant shape changes were observed in the GCD curves before and after cycling. The SEM image of MnO_2-3.3 is shown in Figure S2 after 5000 cycles, and a worm-like structure was observed.

To investigate the pseudocapacitance effect of the spherical δ-MnO_2 nanoflower electrode (MnO_2-3.3), the CV curves were
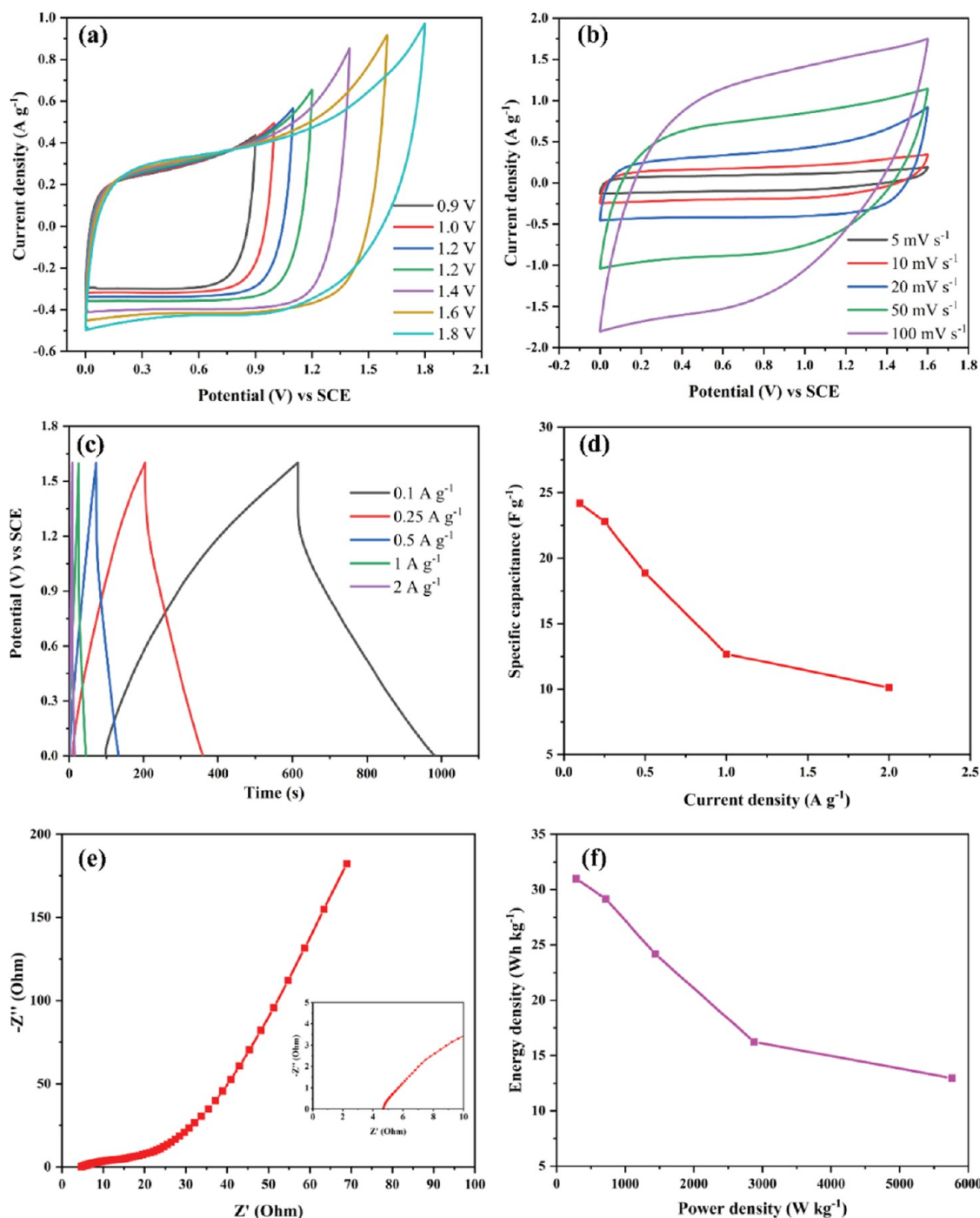
Figure 14. Electrochemical performance of MnO$_2$-3.3-SSC: (a) CV curves at 20 mV s^{-1} under different potential windows; (b) CV curves with different scan rates; (c) GCD curves with different current densities; (d) rate performance; (e) EIS spectra; (f) Ragone plot.

subjected to kinetic analysis at various scanning rates using the following formula[39]

$$i = a\nu^b \qquad (3)$$

where i is the response current (mA) at different scanning rates, ν is the scanning rate (mV s^{-1}), and a and b are constants. The logarithms of both sides of Formula 3 were used to obtain the following formula

$$\log(i) = b\log(\nu) + c \qquad (4)$$

The log(i) to log(ν) was plotted, with b representing the slope. When $b = 0.5$, i was proportional to the square root of ν,

indicating that the charge storage was governed by a diffusion-controlled process and displayed characteristics of battery or bulk-phase pseudocapacitance behavior. In other words, the redox reaction occurred due to the insertion/extraction of electrolyte ions into/from the material and was characterized by slow reaction kinetics. When $b = 1$, it exhibited a purely surface-controlled capacitance behavior, including double-layer capacitance and fast reversible pseudocapacitance occurring on the electrode surface, denoting a fast, electrochemical kinetic process.[40] The fitting results of the reaction kinetics for the spherical δ-MnO$_2$ nanoflowers (MnO$_2$-3.3) are presented in Figure 13(a). The obtained b value of 0.826 suggested that the
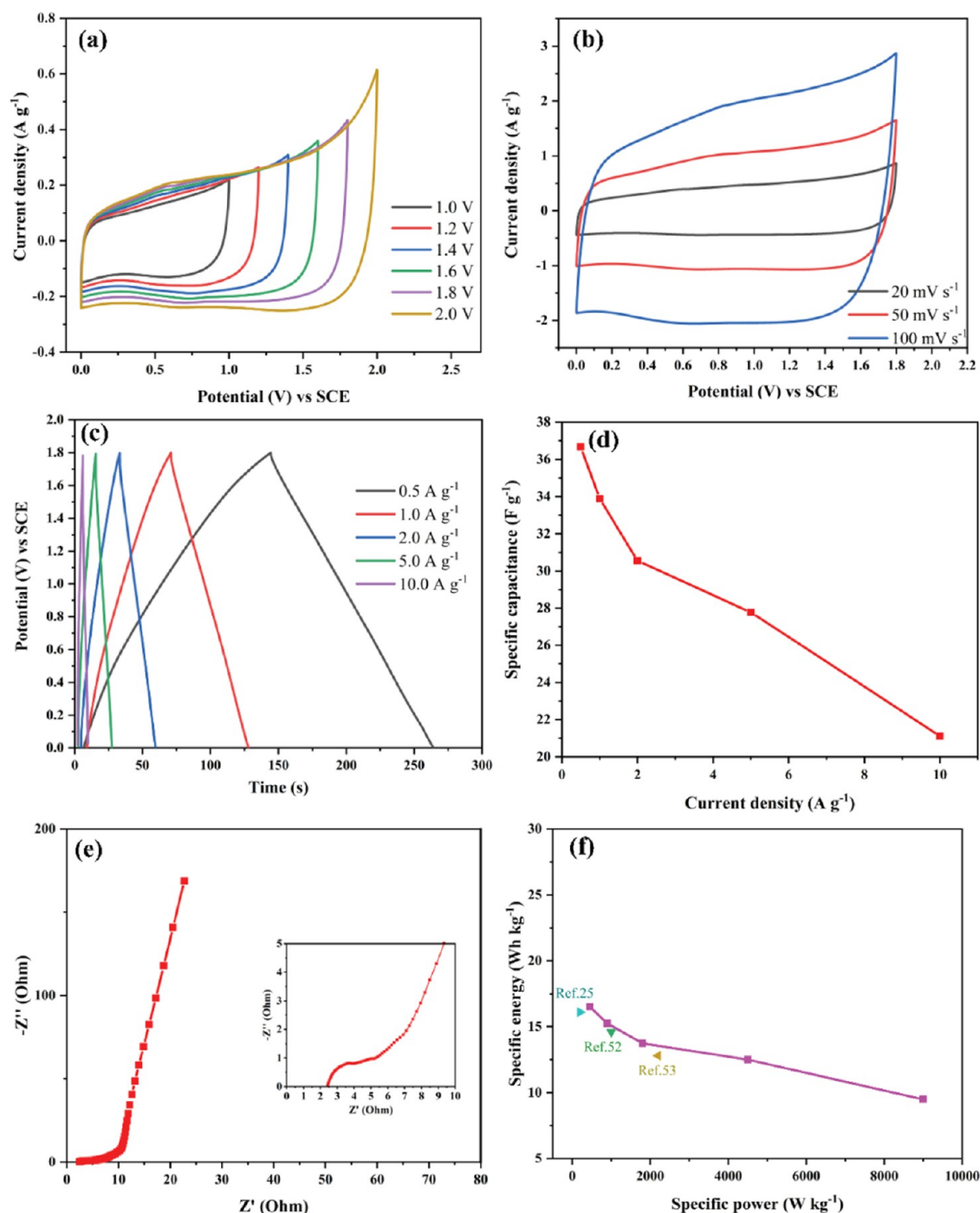
Figure 15. Electrochemical performance of HFC-7// MnO$_2$-3.3-ASC: (a) CV curves at 20 mV s^{-1} under different potential windows; (b) CV curves with different scan rates; (c) GCD curves with different current densities; (d) rate performance; (e) EIS spectra; (f) Ragone plot.

charge storage for the MnO$_2$-3.3 electrode was predominantly governed by a surface-controlled process.

The CV curves were further analyzed to quantitatively distinguish the contribution of capacitance to the current response. A *b* value between 0.5 and 1.0 indicated that the charge storage of the electrode was regulated by a combination of surface- and diffusion-controlled mechanisms. The Dunn method was employed to quantify the contributions of surface-controlled capacity and diffusion-controlled capacity to the overall capacitance,[41,42] and the following Formula can be used.

$$i(\nu) = \kappa_1\nu + \kappa_2\nu^{1/2} \tag{5}$$

Here, $i(\nu)$ denoted the real-time current of the CV test with a scan rate of ν, and $\kappa_1\nu$ and $\kappa_2\nu^{1/2}$ represented the current regulated by surface-controlled capacitance and the current regulated by diffusion-controlled capacitance, respectively. To facilitate analysis and processing, formula 5 was simplified to obtain Formula 6

$$i(\nu)/\nu^{1/2} = \kappa_1\nu^{1/2} + \kappa_2 \tag{6}$$

By determining the values of the κ_1 and κ_2 constants, the proportions of the surface-controlled capacitance and diffusion-

controlled capacitance were quantitatively calculated according to Formula 6 under different scanning speeds. The calculated results are depicted in Figure 13(b). The surface Faraday reaction primarily involved the adsorption and desorption of electrolyte cations on the MnO_2 electrode surface, leading to the manifestation of a surface capacitance effect.[43,44] The process was as follows

$$(MnO_2)_{surface} + C^+ + e^- \leftrightarrow (MnOOC)_{surface} \tag{7}$$
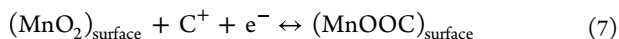
The bulk-phase Faraday reaction primarily relied on the insertion/extraction of electrolyte cations within the MnO_2 electrode, exhibiting a diffusion-controlled effect.[45−47] The process can be described as follows

$$MnO_2 + C^+ + e^- \leftrightarrow MnOOC \tag{8}$$

Due to the significant δ-MnO_2 layer spacing, K^+ can be reversibly inserted or extracted from the interlayer, while the spherical nanoflower structure ensures structural stability. The diffusion-controlled capacitance of the bulk phase accounted for more than 60% at a low scanning rate, which still retained 9.3% even at a high scanning rate (100 mV s^{-1}), indicating that more Faraday charge storage came from the bulk phase of the spherical δ-MnO_2 nanoflower (MnO_2-3.3), resulting in a substantial increase in specific capacity (Formula 8).[36,48,49] Moreover, at high scanning rates, the majority of the capacitance of the spherical δ-MnO_2 nanoflower (MnO_2-3.3) was attributed to surface-controlled capacitance due to its nanosheet structure, which provided a significant specific surface area and numerous active sites, and a large amount of K^+ underwent a rapid reversible redox reaction near the active sites via absorption and desorption, resulting in surface pseudocapacitance (Formula 7).[50]

To further investigate the practicality of a spherical δ-MnO_2 nanoflower (MnO_2-3.3), an aqueous symmetric supercapacitor device (MnO_2-3.3-SSC) was assembled with MnO_2-3.3 as positive and negative electrodes and Na_2SO_4 (1 M) as the electrolyte for electrochemical testing. Figure 14(a) shows the CV curves of MnO_2-3.3-SSC at 20 mV s^{-1} scanning rate under different voltage windows. It can be seen that MnO_2-3.3-SSC displayed a broad potential window range and can still work stably at 1.6 V, while the CV curve became slightly polarized at 1.8 V. Therefore, the voltage window for the electrochemical performance test of MnO_2-3.3-SSC was 1.6 V. The CV curves of the MnO_2-3.3-SSC device at different scanning rates are shown in Figure 14(b). The CV curves presented approximately rectangular and symmetric, without an obvious redox peak, indicating that the charging/discharging process of MnO_2-3.3-SSC was highly reversible. According to the GCD curve (Figure 14(c)), it was calculated that the capacitances of MnO_2-3.3-SSC at the current density of 0.1, 0.25, 0.5, 1, and 2 A g^{-1} were 24.2, 22.8, 18.9, 12.7, and 10.1 F g^{-1}, respectively. The result is depicted in Figure 14(d). Figure 14(e) shows the Nyquist plot of MnO_2-3.3-SSC. The intercept at real axis $R_s = 4.68$ Ω, the charge transfer resistance $R_{ct} = 5.46$ Ω, and smaller semicircle and low-frequency straight line displayed better electrical conductivity and ion diffusion rate of the MnO_2-3.3-SSC. The specific energy (E) and the specific power (P) are two pivotal parameters to evaluate the electrochemical performances of devices. According to the following formulas 9 and 10, the MnO_2-3.3-SSC achieved the maximum specific energy of 8.60 Wh kg^{-1} at 80 W kg^{-1}, which still retained 3.60 Wh kg^{-1} with the specific power of 2600 W kg^{-1}, as shown in the Ragone plot (Figure 14(f)), This value

exceeded the results of some studies of MnO_2-based supercapacitors.[51−53]

$$E = \frac{1}{2}C\Delta V^2 \tag{9}$$

$$P = \frac{E}{\Delta t} \tag{10}$$

In order to further explore the application of spherical δ-MnO_2 nanoflower (MnO_2-3.3) electrode materials in supercapacitor devices, the waste tire pyrolytic activated carbon (HFC-7, our previous work, see ref 5) was used as the negative electrode and MnO_2-3.3 as the positive electrode, and an aqueous asymmetric supercapacitor device (HFC-7//MnO_2-3.3-ASC) was assembled with Na_2SO_4 (1 M) as the electrolyte. CV test was used to estimate the electrochemical potential window of the HFC-7//MnO_2-3.3-ASC, which exhibited a stable potential window up to 2.0 V (Figure 15(a)). The operating potential window of $0-1.8$ V was chosen to avoid polarization for further investigation of the electrochemical performance. Figure 15(b) shows the CV curves of the HFC-7//MnO_2-3.3-ASC at different scanning rates. The CV curves presented a rectangular shape, indicating that the device had ideal capacitance behavior. The shape of the CV curves remained unchanged with the increase of the scanning rate, indicating that HFC-7//MnO_2-3.3-ASC possessed good reversibility. The GCD curves of HFC-7//MnO_2-3.3-ASC (Figures 4−15(c)) exhibited an isosceles triangle with no significant voltage drop, which further indicated that the device had good capacitance behavior and was consistent with CV results. Figure 15(d) shows the rate capability of the HFC-7//MnO_2-3.3-ASC. The specific capacitance was 36.67 F g^{-1} at the current density of 0.5 A g^{-1}, while when the current density was increased by 20 times, the specific capacitance still retained 21.11 F g^{-1}, and the capacitance retention was 57.57%. The device expressed a good rate capability. The Nyquist plot is shown in Figure 15(e), $R_s = 2.42$ Ω, $R_{ct} = 2.86$ Ω, smaller internal resistance, smaller semicircle, and nearly vertical line in the low-frequency region, all of which indicated that the device had smaller resistance and better reaction kinetics than that of MnO_2-3.3-SSC. The maximum specific energy reached 16.5 Wh kg^{-1}, while the maximum specific power reached 9.0 kW kg^{-1}, as depicted in the Ragone plot (Figure 15(f)). This result was comparable and even superior to those reported C/MnO_2 ASC.[24,51,52,54−56]

5. CONCLUSIONS

The δ-MnO_2 was obtained with different molar ratios of $KMnO_4$ to $MnSO_4$ for coprecipitation reaction. The structure, morphology, and electrochemical performance of the as-prepared δ-MnO_2 were tailored by the molar ratio. The spherical δ-MnO_2 nanoflower electrode was synthesized with the molar ration of 3.3, which displayed the largest specific surface area (228.0 m^2 g^{-1}) and the best electrochemical properties. The kinetics of the electrode reaction with the linear potential sweep technique showed that δ-MnO_2 with a nanoflower structure can achieve higher bulk phase utilization. $KMnO_4$ reacted with $MnSO_4$ in the aqueous solution to form MnO_2, which reached the critical nucleation size and aggregated into small particles under Ostwald ripening. Different molar ratios can lead to competition between nucleation control and growth control, resulting in differences in structure, morphology, and properties of as-prepared δ-MnO_2. The as-fabricated asymmetric supercapacitor HFC-7//MnO_2-3.3-ASC exhibited a

remarkable specific energy of 16.5 Wh kg^{-1} at the specific power of 450 W kg^{-1}. The facile strategy to obtain a spherical δ-MnO$_2$ nanoflower and assemble MnO$_2$-based ASC offered great prospects for energy storage due to its low-cost, facile fabrication process and eco-friendly nature.

ASSOCIATED CONTENT

Ⓢ Supporting Information

The Supporting Information is available free of charge at https://pubs.acs.org/doi/10.1021/acsomega.3c09725.

> The molar ratio of KMnO$_4$ and MnSO$_4$·H$_2$O, pore characteristics of MnO$_2$-R electrodes prepared at different molar ratios, the equivalent circuit model of MnO$_2$-3, SEM image of MnO$_2$-3.3 after 5000 cycles (PDF)

AUTHOR INFORMATION

Corresponding Authors

Jianjun Wu − *School of Chemical Engineering & Technology, China University of Mining and Technology, Xuzhou 221116 Jiangsu, P. R. China;* ⓞ orcid.org/0000-0002-0656-8102; Email: jjuw@163.com

Peipei Li − *College of Materials and Chemical Engineering, West Anhui University, Luan 237012 Anhui, P. R. China;* Email: lpp0516@126.com

Authors

Dazhi Zhang − *School of Chemical Engineering & Technology, China University of Mining and Technology, Xuzhou 221116 Jiangsu, P. R. China; Xuzhou College of Industrial Technology, Xuzhou 221114 Jiangsu, P. R. China; Guangxi Key Laboratory of Petrochemical Resource Processing and Process Intensification Technology, School of Chemistry and Chemical Engineering, Guangxi University, Nanning 530004 Guangxi, P. R. China; College of Materials and Chemical Engineering, West Anhui University, Luan 237012 Anhui, P. R. China;* ⓞ orcid.org/0000-0002-2234-4811

Jiamian Dai − *College of Materials and Chemical Engineering, West Anhui University, Luan 237012 Anhui, P. R. China*

Jiajia Zhang − *College of Materials and Chemical Engineering, West Anhui University, Luan 237012 Anhui, P. R. China*

Yixin Zhang − *School of Chemical Engineering & Technology, China University of Mining and Technology, Xuzhou 221116 Jiangsu, P. R. China*

Honglai Liu − *School of Chemistry and Molecular Engineering, East China University of Science and Technology, Shanghai 200237, P. R. China;* ⓞ orcid.org/0000-0002-5682-2295

Yunhui Xu − *Xuzhou College of Industrial Technology, Xuzhou 221114 Jiangsu, P. R. China*

Complete contact information is available at:
https://pubs.acs.org/10.1021/acsomega.3c09725

Author Contributions

D.Z.: Conceptualization, Methodology, Writing—original draft. J.D.: Validation. Y.Z.: Investigation. H.L.: Supervision. Y.X.: Resources. J.W.: Writing—reviewing and editing. P.L.: Visualization, validation.

Notes

The authors declare no competing financial interest.

ACKNOWLEDGMENTS

REFERENCES

(1) Jasna, M.; Manoj, M. P.; Jayaraj, M. K. E. Carbon Based Composites for Supercapacitor Applications. In *Energy Systems in Electrical Engineering*; Springer, 2022.

(2) Zhang, D.; Yang, P.; Zhang, Y.; Liu, H.; Xu, Y.; Wu, J.; Li, P. Facile synthesis of pompon-like manganese dioxide decorated activated carbon composite for supercapacitor electrode. *J. Energy Storage* **2022**, *56*, No. 106134.

(3) Zhang, D.; Zhang, Y.; Liu, H.; Xu, Y.; Wu, J.; Li, P. Effect of pyrolysis temperature on carbon materials derived from reed residue waste biomass for use in supercapacitor electrodes. *J. Phys. Chem. Solids* **2023**, *178*, No. 111318.

(4) Wang, Y.; Zhang, L.; Hou, H.; Xu, W.; Duan, G.; He, S.; Liu, K.; Jiang, S. Recent progress in carbon-based materials for supercapacitor electrodes: a review. *J. Mater. Sci.* **2021**, *56*, 173−200.

(5) Zhang, D.; Ma, Z.; Zhang, Y.; Xu, Y.; Liu, H.; Wu, J.; Li, P. Activated Carbon Tailored by Potassium Hydroxide from Waste Tires as a Supercapacitor Electrode. *ECS J. Solid State Sci. Technol.* **2022**, *11*, No. 061004.

(6) Shin, J.; Seo, J. K.; Yaylian, R.; Huang, A.; Meng, Y. S. A review on mechanistic understanding of MnO$_2$ in aqueous electrolyte for electrical energy storage systems. *Int. Mater. Rev.* **2020**, *65*, 356−387.

(7) Majumdar, D. Review on Current Progress of MnO$_2$-Based Ternary Nanocomposites for Supercapacitor Applications. *ChemElectroChem* **2021**, *8*, 291−336.

(8) Shi, W.; Lee, W. S. V.; Xue, J. Recent Development of Mn-based Oxides as Zinc-Ion Battery Cathode. *ChemSusChem* **2021**, *14*, 1634−1658.

(9) Zhao, X.; Hou, Y.; Wang, Y.; Yang, L.; Zhu, L.; Cao, R.; Sha, Z. Prepared MnO$_2$ with different crystal forms as electrode materials for supercapacitors: experimental research from hydrothermal crystallization process to electrochemical performances. *RSC Adv.* **2017**, *7*, 40286−40294.

(10) Liu, Z.-h.; Ooi, K.; Kanoh, H.; Tang, W.-p.; Tomida, T. Swelling and delamination behaviors of birnessite-type manganese oxide by intercalation of Tetraalkylammonium Ions. *Langmuir* **2000**, *16*, 4154−4164.

(11) Zhao, Y.; Chang, C.; Teng, F.; Zhao, Y.; Chen, G.; Shi, R.; Waterhouse, G. I. N.; Huang, W.; Zhang, T. Defect-Engineered Ultrathin δ-MnO$_2$ Nanosheet Arrays as Bifunctional Electrodes for Efficient Overall Water Splitting. *Adv. Energy Mater.* **2017**, *7*, No. 1700005.

(12) Sunaina; Chand, P.; Joshi, A.; Lal, S.; Singh, V. Effect of hydrothermal temperature on structural, optical and electrochemical properties of α-MnO$_2$ nanostructures for supercapacitor application. *Chem. Phys. Lett.* **2021**, *777*, No. 138742.

(13) Saini, S.; Joshia, A.; Chanda, P. Binder-Free MnO$_2$ Electrodes for Supercapacitor Applications. *ECS Trans.* **2022**, *107* (1), 11847−11856.

(14) Shivakumara, S.; Munichandraiah, N. In-situ preparation of nanostructured α-MnO$_2$/polypyrrole hybrid composite electrode materials for high performance supercapacitor. *J. Alloys Compd.* **2019**, *787*, 1044−1050.

(15) Yin, B.; Zhang, S.; Jiang, H.; Qu, F.; Wu, X. Phase-controlled synthesis of polymorphic MnO$_2$ structures for electrochemical energy storage. *J. Mater. Chem. A* **2015**, *3*, 5722−5729.

(16) Toupin, M.; Brousse, T.; Be'langer, D. Charge Storage Mechanism of MnO$_2$ Electrode Used in Aqueous Electrochemical Capacitor. *Chem. Mater.* **2004**, *16*, 3184−3190.

(17) Tang, C.-L.; Wei, X.; Jiang, Y.-M.; Wu, X.-Y.; Han, L. N.; Wang, K.-X.; Chen, J.-S. Cobalt-Doped MnO2 Hierarchical Yolk−Shell Spheres with Improved Supercapacitive Performance. *J. Phys. Chem. C* **2015**, *119*, 8465−8471.

(18) Wen, Z.; She, W.; Li, Y.; Che, R. Paramecium-like α-MnO2 hierarchical hollow structures with enhanced electrochemical capacitance prepared by a facile dopamine carbon-source assisted shell-swelling etching method. *J. Mater. Chem. A* **2014**, *2*, 20729−20738.

(19) Yao, W.; Wang, J.; Li, H.; Lu, Y. Flexible α-MnO2 paper formed by millimeter-long nanowires for supercapacitor electrodes. *J. Power Sources* **2014**, *247*, 824−830.

(20) Zhai, T.; Xie, S.; Yu, M.; Fang, P.; Liang, C.; Lu, X.; Tong, Y. Oxygen vacancies enhancing capacitive properties of MnO2 nanorods for wearable asymmetric supercapacitors. *Nano Energy* **2014**, *8*, 255−263.

(21) Zhang, Y.; Sun, C.; Lu, P.; Li, K.; Song, S.; Xue, D. Crystallization design of MnO2 towards better supercapacitance. *CrystEngComm* **2012**, *14*, 5892−5897.

(22) Ghodbane, O.; Pascal, J. L.; Favier, F. Microstructural effects on charge-storage properties in MnO2-based electrochemical supercapacitors. *ACS Appl. Mater. Interfaces* **2009**, *1*, 1130−1139.

(23) Grote, F.; Kühnel, R.-S.; Balducci, A.; Lei, Y. Template assisted fabrication of free-standing MnO2 nanotube and nanowire arrays and their application in supercapacitors. *Appl. Phys. Lett.* **2014**, *104*, No. 053904.

(24) Tran, C. C. H.; Santos-Peña, J.; Damas, C. Theoretical and Practical Approach of Soft Template Synthesis for the Preparation of MnO2 Supercapacitor Electrode. *J. Phys. Chem. C* **2018**, *122*, 16−29.

(25) Wang, Y.; Ding, P.; Wang, C. Fabrication and lithium storage properties of MnO2 hierarchical hollow cubes. *J. Alloys Compd.* **2016**, *654*, 273−279.

(26) Jiang, R.; Huang, T.; Liu, J.; Zhuang, J.; Yu, A. A novel method to prepare nanostructured manganese dioxide and its electrochemical properties as a supercapacitor electrode. *Electrochim. Acta* **2009**, *54*, 3047−3052.

(27) Liu, P.; Zhu, Y.; Gao, X.; Huang, Y.; Wang, Y.; Qin, S.; Zhang, Y. Rational construction of bowl-like MnO2 nanosheets with excellent electrochemical performance for supercapacitor electrodes. *Chem. Eng. J.* **2018**, *350*, 79−88.

(28) Zheng, X.; Cai, J.; Cao, Y.; Shen, L.; Zheng, Y.; Liu, F.; Liang, S.; Xiao, Y.; Jiang, L. Construction of cross-linked δ-MnO2 with ultrathin structure for the oxidation of H2S: Structure-activity relationship and kinetics study. *Appl. Catal., B* **2021**, *297*, No. 120402.

(29) Tang, H.; Chen, W.; Li, N.; Hu, Z.; Xiao, L.; Xie, Y.; Xi, L.; Ni, L.; Zhu, Y. Layered MnO2 nanodots as high-rate and stable cathode materials for aqueous zinc-ion storage. *Energy Storage Mater.* **2022**, *48*, 335−343.

(30) Zhai, X. Z.; Qu, J.; Hao, S. M.; Jing, Y. Q.; Chang, W.; Wang, J.; Li, W.; Abdelkrim, Y.; Yuan, H.; Yu, Z. Z. Layered Birnessite Cathode with a Displacement/Intercalation Mechanism for High-Performance Aqueous Zinc-Ion Batteries. *Nano-Micro Lett.* **2020**, *12*, No. 56.

(31) Coasne, B.; Grosman, A.; Ortega, C.; Simon, M. Adsorption in noninterconnected pores open at one or at both ends: a reconsideration of the origin of the hysteresis phenomenon. *Phys. Rev. Lett.* **2002**, *88*, No. 256102.

(32) Lang, X.; Hirata, A.; Fujita, T.; Chen, M. Nanoporous metal/oxide hybrid electrodes for electrochemical supercapacitors. *Nat. Nanotechnol.* **2011**, *6*, 232−236.

(33) Julien, C. Raman spectra of birnessite manganese dioxides. *Solid State Ionics* **2003**, *159*, 345−356.

(34) Zhu, S.; Huo, W.; Liu, X.; Zhang, Y. Birnessite based nanostructures for supercapacitors: challenges, strategies and prospects. *Nanoscale Adv.* **2020**, *2*, 37−54.

(35) Tebo, B. M.; Bargar, J. R.; Clement, B. G.; Dick, G. J.; Murray, K. J.; Parker, D.; Verity, R.; Webb, S. M. BIOGENIC MANGANESE OXIDES: Properties and Mechanisms of Formation. *Annu. Rev. Earth Planet. Sci.* **2004**, *32*, 287−328.

(36) Zhu, S.; Li, L.; Liu, J.; Wang, H.; Wang, T.; Zhang, Y.; Zhang, L.; Ruoff, R. S.; Dong, F. Structural Directed Growth of Ultrathin Parallel Birnessite on beta-MnO(2) for High-Performance Asymmetric Supercapacitors. *ACS Nano* **2018**, *12*, 1033−1042.

(37) Pandit, B.; Goda, E. S.; Ubaidullah, M.; Shaikh, S. F.; Nakate, U. T.; Khedulkar, A. P.; Rana, A. u. H. S.; Kumar, D.; Doong, R.-a. Hexagonal δ-MnO2 nanoplates as efficient cathode material for potassium-ion batteries. *Ceram. Int.* **2022**, *48*, 28856−28863.

(38) Musil, M.; Choi, B.; Tsutsumi, A. Morphology and Electrochemical Properties of α-, β-, γ-, and δ-MnO2 Synthesized by Redox Method. *J. Electrochem. Soc.* **2015**, *162*, A2058−A2065.

(39) Qiu, G.; Guo, Y.; Zhang, Y.; Zhao, X.; Xu, J.; Guo, S.; Guo, F.; Wu, J. Construction of N, O Codoped Petal-like Hierarchical Porous Carbon with an Ultrahigh Specific Surface from Waste Bamboo for High-Performance Supercapacitors. *Ind. Eng. Chem. Res.* **2022**, *61*, 16034−16049.

(40) Xu, W.; Sun, C.; Zhao, K.; Cheng, X.; Rawal, S.; Xu, Y.; Wang, Y. Defect engineering activating (Boosting) zinc storage capacity of MoS2. *Energy Storage Mater.* **2019**, *16*, 527−534.

(41) Wang, Y.; Song, Y.; Xia, Y. Electrochemical capacitors: mechanism, materials, systems, characterization and applications. *Chem. Soc. Rev.* **2016**, *45*, 5925−5950.

(42) Brezesinski, T.; Wang, J.; Tolbert, S. H.; Dunn, B. Ordered mesoporous α-MoO3 with iso-oriented nanocrystalline walls for thin-film pseudocapacitors. *Nat. Mater.* **2010**, *9*, 146−151.

(43) Bai, X.; Tong, X.; Gao, Y.; Zhu, W.; Fu, C.; Ma, J.; Tan, T.; Wang, C.; Luo, Y.; Sun, H. Hierarchical multidimensional MnO2 via hydrothermal synthesis for high performance supercapacitors. *Electrochim. Acta* **2018**, *281*, 525−533.

(44) Xia, T.; Wang, Q.; Wu, W.; Ao, C.; Zheng, Z.; Lu, C.; Chen, Z.; Zhang, W. Fabrication and characterization of MnO2-Coated carbon fabrics from silk for shape-editable supercapacitors. *J. Alloys Compd.* **2021**, *854*, No. 157289.

(45) Brousse, T.; Toupin, M.; Dugas, R.; Athouël, L.; Crosnier, O.; Bélanger, D. Crystalline MnO2 as Possible Alternatives to Amorphous Compounds in Electrochemical Supercapacitors. *J. Electrochem. Soc.* **2006**, *153* (12), A2171−A2180.

(46) Kuo, S.; Wu, N. Investigation of Pseudocapacitive Charge-Storage reaction of MnO2·nH2O Supercapacitors in Aqueous Electrolytes. *J. Electrochem. Soc.* **2006**, *153* (7), A1317−A1324.

(47) Cui, P.; Zhang, Y.; Cao, Z.; Liu, Y.; Sun, Z.; Cheng, S.; Wu, Y.; Fu, J.; Xie, E. Plasma-assisted lattice oxygen vacancies engineering recipe for high-performing supercapacitors in a model of birnessite-MnO2. *Chem. Eng. J.* **2021**, *412*, No. 128676.

(48) Zhu, Y.-P.; Xia, C.; Lei, Y.; Singh, N.; Schwingenschlögl, U.; Alshareef, H. N. Solubility contrast strategy for enhancing intercalation pseudocapacitance in layered MnO2 electrodes. *Nano Energy* **2019**, *56*, 357−364.

(49) Wang, H.; Fan, R.; Miao, J.; Chen, J.; Mao, S.; Deng, J.; Wang, Y. Oxygen vacancies on the surface of HxWO3−y for enhanced charge storage. *J. Mater. Chem. A* **2018**, *6*, 6780−6784.

(50) Chu, J.; Lu, D.; Ma, J.; Wang, M.; Wang, X.; Xiong, S. Controlled growth of MnO2 via a facile one-step hydrothermal method and their application in supercapacitors. *Mater. Lett.* **2017**, *193*, 263−265.

(51) Liu, T.; Jiang, C.; You, W.; Yu, J. Hierarchical porous C/MnO2 composite hollow microspheres with enhanced supercapacitor performance. *J. Mater. Chem. A* **2017**, *5*, 8635−8643.

(52) Gao, H.; Xiao, F.; Ching, C. B.; Duan, H. High-performance asymmetric supercapacitor based on graphene hydrogel and nano-structured MnO2. *ACS Appl. Mater. Interfaces* **2012**, *4*, 2801−2810.

(53) Kalubarme, R. S.; Jadhav, H. S.; Park, C.-J. Electrochemical characteristics of two-dimensional nano-structured MnO2 for symmetric supercapacitor. *Electrochim. Acta* **2013**, *87*, 457−465.

(54) Lv, H.; Yuan, Y.; Xu, Q.; Liu, H.; Wang, Y.-G.; Xia, Y. Carbon quantum dots anchoring MnO2 /graphene aerogel exhibits excellent performance as electrode materials for supercapacitor. *J. Power Sources* **2018**, *398*, 167−174.

(55) Li, J.; Yin, M.; Guo, C.; Zhang, H.; Li, T.; Wang, H.; Wei, Y.; Hou, L.; Jia, C. Belt-like MnO2 cathode to enable high energy density and ultra-stable aqueous asymmetric supercapacitor. *Surf. Coat. Technol.* **2019**, *359*, 175−182.

(56) Li, H.; Zhang, X.; Ding, R.; Qi, L.; Wang, H. Facile synthesis of mesoporous MnO_2 microspheres for high performance $AC//MnO_2$ aqueous hybrid supercapacitors. *Electrochim. Acta* **2013**, *108*, 497−505.